Atmos. Meas. Tech. Discuss., 7, 8465–8519, 2014
www.atmos-meas-tech-discuss.net/7/8465/2014/
doi:10.5194/amtd-7-8465-2014

Atmospheric Measurement Techniques Discussions

Hydrometeor classification from polarimetric radar measurements: a clustering approach

J. Grazioli[1], **D. Tuia**[2], **and A. Berne**[1]

[1]Environmental Remote Sensing Laboratory (LTE), École Polytechnique Fédérale de Lausanne (EPFL), Lausanne, Switzerland
[2]Laboratory of Geographic Information Systems (LASIG), École Polytechnique Fédérale de Lausanne (EPFL), Lausanne, Switzerland

Received: 24 July 2014 – Accepted: 1 August 2014 – Published: 19 August 2014

Correspondence to: A. Berne (alexis.berne@epfl.ch)

Published by Copernicus Publications on behalf of the European Geosciences Union.

Abstract

A data-driven approach to the classification of hydrometeors from measurements collected with polarimetric weather radars is proposed. In a first step, the optimal number n_{opt} of hydrometeor classes that can be reliably identified from a large set of polarimetric data is determined. This is done by means of an unsupervised clustering technique guided by criteria related both to data similarity and to spatial smoothness of the classified images. In a second step, the n_{opt} clusters are assigned to the appropriate hydrometeor class by means of human interpretation and comparisons with the output of other classification techniques. The main innovation in the proposed method is the unsupervised part: the hydrometeor classes are not defined a-priori, but they are learned from data. The proposed approach is applied to data collected by an X-band polarimetric weather radar during two field campaigns (totalling about 3000 h of precipitation). Seven hydrometeor classes have been found in the data set and they have been associated to drizzle (DZ), light rain (LR), heavy rain (HR), melting snow (MS), ice crystals/small aggregates (CR), aggregates (AG), rimed particles (RI).

1 Introduction

Hydrometeor classification (HC) from weather radar data refers to a family of techniques and algorithms that retrieve a qualitative information about precipitation: the dominant hydrometeor type within a given sampling volume, where the term "dominant" is used to underline that the actual hydrometeor content is usually a mixture. These methods use as input a set of quantitative measurements provided by the radar itself and some additional information coming from external sources such as vertical profiles of temperature or estimates of the 0 °C isotherm height.

The classification is conducted at the spatial scale of the radar resolution volume and its inputs are usually a set of polarimetric variables like horizontal reflectivity Z_H,

AMTD
7, 8465–8519, 2014

differential reflectivity Z_{DR}, correlation coefficient ρ_{hv} and specific differential phase K_{dp}[1] (see Bringi and Chandrasekar, 2001; Berne and Krajewski, 2013, for definitions).

The most modern HC techniques require dual-polarization (and Doppler) capabilities. These allow to acquire with a single instrument multiple measurements, each one sensitive to distinct characteristics of precipitation, and facilitate the interpretation of many microphysical processes (e.g. Seliga and Bringi, 1976; Jameson, 1983; Vivekanandan et al., 1994; Ryzhkov et al., 2005; Bechini et al., 2013; Schneebeli et al., 2013).

Different HC algorithms are available for S-band (Straka et al., 2000; Liu and Chandrasekar, 2000), C-band (Marzano et al., 2007; Dolan et al., 2013) and X-band (Dolan and Rutledge, 2009; Snyder et al., 2010; Marzano et al., 2010) radar frequencies. Recently, after years of improvements, HC also became a common product provided operationally by national meteorological services (e.g. Gourley et al., 2007; Al-Sakka et al., 2013; Chandrasekar et al., 2013).

Most HC methods are based on similar principles: they start by selecting the number and type of hydrometeor classes undergoing classification. Then, through scattering simulations, the theoretical radar observations associated with these hydrometeor classes are reconstructed. Finally, actual observations are associated (labeled) with the appropriate class according to their degree of similarity with the sets of simulations available. This last step is usually conducted by means of a fuzzy logic input-output association (e.g. Dolan and Rutledge, 2009), or by means of Bayesian (Marzano et al., 2010) and neural network (Liu and Chandrasekar, 2000) techniques. In some cases these relations rely entirely on the simulation framework available (e.g., Dolan and Rutledge, 2009). In other cases, instead, they are adapted and modified in order to adequately reproduce actual observations (e.g. Marzano et al., 2007), or according to empirically-based constraints (e.g. Al-Sakka et al., 2013).

[1] In the present manuscript we denote with capital subscripts the variables expressed in dB (Z_H and Z_{DR}), and with lower-case subscripts the other ones (ρ_{hv}, K_{dp}, Φ_{dp}, Ψ_{dp}).

AMTD
7, 8465–8519, 2014

The typical HC techniques mentioned above have become a state-of-the-art approach, stable and robust enough to be implemented operationally. However it is important to underline that this approach has some limitations, since it relies on strong assumptions. First, the choice of the hydrometeor classes in the classification scheme is mostly subjective. Secondly, the scattering simulations (e.g. Mishchenko et al., 1996), which are usually very accurate for rainfall, are largely uncertain for ice-phase hydrometeors, because of the complex geometries, dielectric properties and particle size distributions of ice particles (Tyynela et al., 2011). Finally, it is not easy to take into account the accuracy of actual radar measurements when comparing simulations and observations. In the present paper we propose a different approach to HC, in which the classifier is built on actually measured radar data instead of on numerical simulations.

A clustering technique, i.e., a technique that is used to find patterns (groups) in data sets in an unsupervised way (see Jain et al., 1999; Xu and Wunsch, 2005; Von Luxburg, 2007, for a complete overview) is applied to a database of precipitation measurements collected by an X-band dual-polarization radar. An optimal partition of these data into n_{opt} separate groups is found as a trade-off between data similarity (in terms of polarimetric variables), and spatial smoothness of the partition. The content of these groups is then interpreted a-posteriori, and a hydrometeor class is assigned to each of them.

The manuscript is structured as follows. Section 2 provides some background on clustering algorithms and Sect. 3 presents the polarimetric data employed in the study. Section 4 describes the unsupervised part of the classification method and Sect. 5 is devoted to the identification of the optimal number of clusters in the data set. Section 6 deals with the labelling of the n_{opt} clusters identified, and Sect. 7 presents the summary, discussion and conclusions.

2 Background on clustering techniques

The proposed approach to HC is data-driven. The first two necessary steps are therefore to identify groups (clusters) in the available data set, and then to define as

AMTD
7, 8465–8519, 2014

objectively as possible the optimal number of these groups. In this section we provide some background on the clustering methods that will be employed in the following.

2.1 Hierarchical data clustering

We define as unsupervised data clustering techniques all techniques that aim at organizing a given set of objects (observations) in a certain number of groups (clusters). The shape (or functional form) of these groups, as well as their number, is unknown a-priori (Jain et al., 2000).

We consider here a particular type of clustering technique: the agglomerative hierarchical clustering (Ward, 1963, AHC hereafter). AHC is a step-wise approach that is used to group a set of N_D objects into n_c clusters ($n_c \leq N_D$) in a way that objects belonging to the same cluster are more similar to each other than to those belonging to the others. The technique is called agglomerative because at a step i:

$$n_c^i = N_D - i. \quad (1)$$

This means that at the initial step ($i = 0$) single objects populates the clusters, while at each step two objects (the most similar) are merged together, thus reducing the total number of clusters by one. The method is nested, in the sense that once two samples are grouped in the same cluster, they remain clustered in all the following levels of the hierarchy.

In order to define which objects are the most similar, two criteria need to be defined (Xu and Wunsch, 2005): (i) a metric i.e., a measure of distance between objects and (ii) a merging rule. At each step i the pair of objects that are situated at the closest distance (according to a certain merging rule) are merged together.

AMTD
7, 8465–8519, 2014

2.2 Distance metric

Let $\boldsymbol{x}$ and $\boldsymbol{y}$ be two objects, defined in a d dimensional space. They have therefore d components:

$$\boldsymbol{x} = \{\boldsymbol{x}[1], \ldots \boldsymbol{x}[d]\}$$
$$\boldsymbol{y} = \{\boldsymbol{y}[1], \ldots \boldsymbol{y}[d]\}$$

A list of common distance metrics $D(\boldsymbol{x}, \boldsymbol{y})$ between $\boldsymbol{x}$ and $\boldsymbol{y}$ is provided in Table 1. Each of these metrics is designed to capture a particular type of similarity between pairs of objects. To cite a few, the "Minkowski Distance"[2], is a good index of similarity when all the d components of $\boldsymbol{x}$ and $\boldsymbol{y}$ have the same order of magnitude, while the "Correlative" distance is less affected by unbalanced components but might be ill-defined when d is small.

2.3 Merging rule

The second concept to introduce is the merging rule. A merging rule defines the criteria that an object $\boldsymbol{x}$, or a cluster of objects C_I (a group of objects $\boldsymbol{x} \in C_I$), has to satisfy in order to be merged with another cluster C_J. In other words, it generalizes the concept of distance between single objects of Table 1 to distances between two clusters, or between a cluster and a single object. The merging rules tested in the present work include the single linkage (SL), complete linkage (CL), weighted pairwise average (WPA, sometimes also defined as WPGMA), and weighted centroid (WC) distance (Jain and Dubes, 1988).

[2]Note that this distance reduces to the well known Euclidean distance (if $p = 2$) and the "City-block" distance (if $p = 1$), according to the notation of Table 1.

AMTD
7, 8465–8519, 2014

– SL defines the distance between two clusters (C_I and C_J) as the minimum distance between couples of objects belonging to these clusters:

$$D(C_I, C_J) = \min_{\boldsymbol{x} \in C_I, \boldsymbol{y} \in C_J} D(\boldsymbol{x}, \boldsymbol{y}) \tag{2}$$

– CL selects the maximum distance between objects:

$$D(C_I, C_J) = \max_{\boldsymbol{x} \in C_I, \boldsymbol{y} \in C_J} D(\boldsymbol{x}, \boldsymbol{y}) \tag{3}$$

– WPA defines the distance between objects as the average distance between couples of objects belonging to the two clusters, weighted by the number of object of each sub-cluster. In this case the definition of distance between clusters, employed as merging rule, is recursive. As an example, given $C_I = C_K \cup C_L$:

$$D(C_I, C_J) = D(C_{K \cup L}, C_J) = \frac{n_K D(C_K, C_J) + n_L D(C_L, C_J)}{n_K + n_L} \tag{4}$$

where n_K and n_L are the number of objects contained in the clusters C_K and C_L, respectively.

– WC defines the distance between clusters as the distance between the (weighted) centroids of each cluster. The centroid is the centre of mass of a cluster C_I. It is computed as the average position of all the sub-clusters $C_K \subset C_I$, weighted by the number of objects in each C_K. Thus:

$$D(C_I, C_J) = D(\overline{\boldsymbol{x}}_{C_I}, \overline{\boldsymbol{x}}_{C_J}) \tag{5}$$

where $\overline{\boldsymbol{x}}_{C_I}$ is the weighted centroid of cluster C_I, defined as:

$$\overline{\boldsymbol{x}}_{C_I} = \frac{\sum_{C_K \subset C_I} n_K \sum_{\boldsymbol{x} \in C_K} \boldsymbol{x}}{n_I} \tag{6}$$

AMTD
7, 8465–8519, 2014

Even though different distance metrics and different merging criteria can be defined, all hierarchical cluster methods start with N objects distributed into N clusters, and they end with N objects in one single cluster. The key point of any clustering method is therefore the selection of the optimal intermediate partition, named n_{opt}, between the starting and the ending point. A universally applicable criterion to perform this choice does not exist, and the selection is usually based both on quantitative cluster quality indices and on the available prior knowledge about the data undergoing clustering (Kovács and Iváncsy, 2006; Wilks, 2011).

3 Data and processing

The present section provides a description of the data employed in the following analysis, and some details about data processing.

3.1 Data source

The polarimetric radar data considered here were collected with an X-band dual-polarization Doppler weather radar (MXPol), whose characteristics are summarized in Table 2.

During any measurement period MXPol was deployed at single locations for the whole duration of the measurements. This ensures that data collected during different days are referenced with respect to the exact same location. The pointing accuracy of the mechanical antenna was adjusted by means of a Sun-tracking scan, following the approach of Muth et al. (2012).

In the present work we employ radar data collected during two field deployments. The first one took place in Davos (CH), in the Swiss Alps, from September 2009 to July 2011. The radar was deployed at 2133 m a.s.l. on a ski slope dominating the valley of Davos, as shown in Fig. 1a. The altitude of the deployment site allowed to collect many observations of ice-phase precipitation when the radar itself was located above

AMTD
7, 8465–8519, 2014

the melting layer, and therefore not suffering from liquid-water signal attenuation. Given the complex topography, the scanning sequence included multiple Plan Position Indicator (PPI) sector scans over the valley of Davos, at elevation angles ranging from 9° to 27°, a Range Height Indicator (RHI), and a vertically-pointing PPI used for the calibration of the differential reflectivity Z_{DR}.

The second field deployment took place in the Ardèche region (FR) from September to November 2012, at an altitude of 605 m a.s.l. This deployment was part of the HyMeX experiment (www.hymex.org, Bousquet et al., 2014). Stratiform and convective Mediterranean precipitation events were sampled during this campaign. The scanning sequence in this case included large sector scans (spanning 200° in azimuth) conducted at elevations ranging from 3.5° to 10° (Fig. 1b). Additionally, RHIs towards different directions as well as a Z_{DR} calibration zenithal PPI were collected within each scanning sequence.

3.2 Polarimetric data

The polarimetric variables calculated from the measurements of MXPol and employed in the following analysis are: Z_H [dBZ], Z_{DR} [dB], K_{dp} [° km^{-1}] and ρ_{hv} [–].

PPI data of Z_H and Z_{DR} collected in rain are corrected for attenuation using the relations linking K_{dp}, Z_H, specific horizontal attenuation α_H [dBZ km^{-1}], and differential attenuation α_{dr} [dB km^{-1}] according to the method of Testud et al. (2000). The power laws between these variables are parametrized using disdrometer measurements for the data collected in France (Fig. 1b) and using simulated realistic drop size distribution fields (Schleiss et al., 2012) for the data collected in Switzerland. The set of observations corresponding to events during which the radar was located above the melting layer were not corrected for attenuation, assuming the attenuation in dry snow to be negligible.

K_{dp} is estimated from the total differential phase shift Ψ_{dp} [°] using a method based on Kalman filtering (Schneebeli et al., 2014). The approach is designed to guarantee

AMTD
7, 8465–8519, 2014

the independence between K_{dp} estimates and other polarimetric variables, and to capture the fine-scale variations of K_{dp}. All the polarimetric variables are censored with a mask of signal-to-noise ratio SNR > 8 dB, and all the radar resolutions volumes potentially contaminated by ground clutter are censored as well.

4 Clustering of polarimetric radar data

Hierarchical clustering is applied to radar observations (objects) $\boldsymbol{x}$, defined in the multi-dimensional space of the polarimetric variables. Here we present in detail our clustering approach and we apply it to the database of Sect. 3.

4.1 Data preparation

The data object $\boldsymbol{x}$ is a five dimensional vector defined for each valid radar resolution volume. The components of $\boldsymbol{x}$ are therefore:

$$\boldsymbol{x} = \{Z_H, Z_{DR}, K_{dp}, \rho_{hv}, \Delta z\}. \quad (7)$$

The last component ($\boldsymbol{x}[5] = \Delta z$) is not a polarimetric variable and it is defined as:

$$\Delta z_i = z_i - z_{0^\circ} \quad (8)$$

where z_i [m] is the altitude above sea level of the ith resolution volume, and z_{0° is the estimated altitude of the 0 °C isotherm, taken as a reference. A positive Δz refers to a measurement collected at temperature ranges where ice-phase hydrometeors are expected, while a negative one to a measurement likely taken in liquid-phase precipitation. This variable is used as a prior information for the clustering algorithm, in order to take into account the approximate environmental conditions associated to each measurement. z_{0° is estimated by means of linear interpolation of the data coming from ground-based weather stations located at different altitudes and at a distance ≤ 40 km

AMTD
7, 8465–8519, 2014

from the radar location. It can also be estimated from radar data directly, when a melting layer is sampled.

The vector $\boldsymbol{x}$ is not yet suitable to undergo cluster analysis. Two different issues need to be tackled.

1. The first issue is related to the distribution of K_{dp} values: at X-band, K_{dp} ranges approximately from -1 to $25^{\circ}\,km^{-1}$ (e.g. Dolan and Rutledge, 2009; Otto and Russchenberg, 2011) but its probability distribution, calculated over a large set of observations, is positively skewed with typical modal values below $0.5^{\circ}\,km^{-1}$. This issue is tackled by log-transforming K_{dp} values before performing the cluster analysis. Values of K_{dp} lower than $0.005^{\circ}\,km^{-1}$ (corresponding in rain to $R \approx 0.2\,mm\,h^{-1}$, Otto and Russchenberg, 2012) are set to $0.005^{\circ}\,km^{-1}$ and K_{dp} is then transformed with a natural logarithm. By proceeding this way, negative K_{dp} values with actual physical meaning (e.g., vertically alligned ice, Dolan and Rutledge, 2009) might be lost. However, it was verified that in the data set employed the occurrence of negative K_{dp} values ($K_{dp} < -0.5^{\circ}\,km^{-1}$) is very low ($< 0.5\,\%$). Furthermore, slightly negative values ($-0.5 < K_{dp} < 0^{\circ}\,km^{-1}$), cannot be discriminated from positive ones because of the uncertainties associated with the estimation of K_{dp} (see Grazioli et al., 2014a, for the expected boundaries of accuracy around K_{dp}).

2. The different components of $\boldsymbol{x}$, due to the differences in their units, have typical range of values that differ by several orders of magnitude. For instance, Z_H can vary over tens of dBZ, while Z_{DR} and K_{dp} are smaller by one order of magnitude and ρ_{hv} even by two orders of magnitude. This issue is tackled by means of data standardization (stretching). Even though a classical approach would be to use a z-score transformation, based on mean and standard deviation of a sample of data (e.g. Wilks, 2011), we selected a method based on minimum and maximum boundaries, that allows to pre-select physically relevant thresholds. The

AMTD
7, 8465–8519, 2014

components $\boldsymbol{x}[i]^*$ of the standardized data are obtained as:

$$\boldsymbol{x}[i]^* = \frac{\boldsymbol{x}[i] - \boldsymbol{x}_{\min}[i]}{\boldsymbol{x}_{\max}[i] - \boldsymbol{x}_{\min}[i]} \qquad i \in \{1,2,3,4\} \tag{9}$$

where $\boldsymbol{x}_{\min}[i]$ ($\boldsymbol{x}_{\max}[i]$) is a minimum (maximum) value assigned to each polarimetric variable. The boundaries employed in the present study are: −10 to 60 dBZ for Z_H, −1.5 to 5 dB for Z_{DR}, −5.3 to 3 log(° km^{-1}) for log(K_{dp}), 0.7 to 1 [–] for ρ_{hv} (Δz is considered in the next paragraph). Variations on the order of ±20 % around the proposed boundaries have a negligible impact on the results presented in Sect. 5.

Δz is stretched within a smaller range of variation in the following way:

$$\boldsymbol{x}[5]^* = \begin{cases} 0 & \text{if } \Delta z \le -400; \\ \kappa & \text{if } \Delta z > 400; \\ f(\Delta z) \times \kappa & \text{if } -400 < \Delta z \le 400 \end{cases} \tag{10}$$

$0 < \kappa \le 1$.

κ is a scaling factor and $f(\Delta z)$ denotes any monotonically increasing functional form that gives continuity to Eq. (10). Gaussian, sigmoid and logistic functions have been tested and appeared to be adequate. The reason behind a different standardization for Δz is to reduce the weight of this non-polarimetric input in the clustering process: this parameter is intended only to flag positive and negative temperatures in a quasi-binary way and not to substitute the information provided by the polarimetric variables (therefore κ is kept strictly ≤ 1). κ factors ranging between 0.3 and 0.9 lead to similar outputs, and an intermediate value of 0.5 was used.

With the standardization detailed in Eqs. (9) and (10), the radar observations collected at each resolution volume are summarized by the observation vector $\boldsymbol{x}^*$, whose entries are now expressed in a similar order of magnitude.

AMTD
7, 8465–8519, 2014

4.2 Subset undergoing clustering analysis

Agglomerative clustering algorithms are generally computationally expensive, because full distance matrices among all samples (and then groups) to be clustered are computed at each step of the hierarchical aggregation chain. Therefore we opted for the definition of the clusters using a representative subset of the data and then to assign the whole dataset to these clusters using a nearest cluster rule (e.g., Volpi et al., 2012).

About 50 precipitation events belonging to the data set of Sect. 3 were manually selected. These events cover the range of precipitation types observed with MXPol, and they are assumed to be a representative sample of mid-latitude temperate precipitation.

A random portion of data is taken from each of these 50 precipitation events, from PPI scans conducted at elevation angles between 3.5° and 10° (free of ground clutter contamination). A total of 20 000 observations $\boldsymbol{x}^*$ are extracted and are used as input of the subsequent cluster analysis. Evaluation of the results over multiple choices of the initial random selection, as well as the exclusion of some manually selected precipitation events showed that the random sampling did not affect the outcome of the clustering technique presented in the next section.

4.3 Clustering algorithm: data similarity and spatial smoothness

An AHC is applied to the polarimetric data set of $\boldsymbol{x}^*$ objects in order to obtain an optimal partition of the data into a set of clusters.

The technique is a trade-off between purely data-driven clustering, as it was described in Sect. 2a (i.e., that only looks for similarity in the 5-D feature space of $\boldsymbol{x}^*$) and spatial smoothness of the partition in the physical space. In other words, groups of precipitation types should both contain objects that are similar among each other (data-wise) and that exhibit spatial consistency, since we assume spatial smoothness of the geographic distribution of precipitation types. Here, and in the following, we will refer to an Euclidean distance metric and WPA linkage. Similar results can be obtained with correlative distance metrics, and/or WC linkage criteria. The method developed

AMTD
7, 8465–8519, 2014

in the present paper is sketched in the flow chart of Fig. 2. Panel a of the figure is explained step by step in the following sections.

4.3.1 Step1 (Fig. 2a1)

Initially the 20 000 selected objects populate $n_c = 20\,000$ clusters. A first hierarchical aggregation is conducted on the data, until reaching a number of 1 000 clusters in the dataset. This step aims at merging the most similar objects before proceeding with more computationally expensive calculations.

4.3.2 Step2 (Fig. 2a2)

Given the remaining $n_c = 1000$ clusters, referred to as C_L ($L = 1, \ldots n_c$), we proceed to the classification of the entire PPI images from which the original 20 000 objects were extracted. Let $\boldsymbol{x}_p^* \notin C_L$ ($L = 1, \ldots n_c$) be an object taken from one of the PPI images, and not belonging to any cluster C_L. This object is now classified into one of the n_c clusters available, specifically the one related to the minimal distance to it (according to the given merging rule). We proceed until all the objects of the PPI images are classified into one of the n_c clusters available. An example of a classified PPI image, corresponding to $n_c = 7$ can be found in Fig. 7.

At this point, we evaluate the spatial smoothness of the partition into n_c clusters. Each object $\boldsymbol{x}_p^*$ has been assigned to a cluster C_M ($1 < M \leq n_c$). We define now a local spatial smoothness index (SSI) associated with $\boldsymbol{x}_p^*$. This index evaluates the spatial consistency of the classification of an object with respect to the classification of neighbouring objects:

$$\mathrm{SSI}(\boldsymbol{x}_p^*, C_M) = \frac{1}{n_{\mathrm{NN}}} \sum_{i(p)=1}^{n_{\mathrm{NN}}} \delta_{i(p)} \tag{11}$$

AMTD
7, 8465–8519, 2014

where

$$\delta_{i(p)} = \begin{cases} 0 & \text{if } \boldsymbol{x}^*_{i(p)} \notin C_M \\ 1 & \text{if } \boldsymbol{x}^*_{i(p)} \in C_M \end{cases}$$

where n_{NN} (number of Nearest Neighbours) is the number of nearest objects considered in the construction of SSI, and $\boldsymbol{x}^*_{i(p)}$ indicates the ith nearest object of $\boldsymbol{x}^*_p$. In the present work $n_{\mathrm{NN}} = 4$, and very similar results are obtained for $n_{\mathrm{NN}} = 2, 4, 8$. The larger n_{NN}, the further the smoothing effect for the spatial regularization will reach. The identification of the nearest neighbours is performed in polar coordinates and therefore the nearest object refers to the nearest radar resolution volume. Figure 3 illustrates this concept, by labelling the 8 nearest neighbours of a resolution volume centered on sample "0" on the figure.

SSI ranges between 0 and 1. If all the n_{NN} objects belong to cluster C_M, then SSI is equal to 1. More generally, SSI is also defined if $\boldsymbol{x}^*_p \in C_Q$ ($Q \neq M$). In this case the index quantifies the occurrence of C_M objects around $\boldsymbol{x}^*_p$, rather than the spatial smoothness around it.

SSI indices are calculated for each $\boldsymbol{x}^*_p$ and they are summarized in a $n_c \times n_c$ matrix $\mathbf{M}$, hereafter called spatial smoothness matrix. The elements $M_{I,J}$ of $\mathbf{M}$ are defined as:

$$M_{I,J} = \sum_{p=1}^{N_I} \mathrm{SSI}(\mathbf{x_p}^*, C_J) \tag{12}$$

where N_I is the total number of objects $\boldsymbol{x}^*_p$ satisfying the condition $\boldsymbol{x}^*_p \in C_I$. The matrix $\mathbf{M}$ is conceptually similar to a confusion matrix, commonly used to evaluate the goodness of categorical classifications (e.g. Wilks, 2011). Diagonal entries $M_{I,I}$ quantify the global spatial smoothness of the cluster C_I, while the off-diagonal terms $M_{I,J}$ ($I \neq J$) quantify the probability of objects belonging to a cluster C_I to be surrounded by objects of the cluster C_J.

AMTD
7, 8465–8519, 2014

In analogy with a confusion matrix, the information contained in **M** can be further summarized by means of quality indices. As an example, Cohen's Kappa can be used to evaluate the global smoothness of a partition of the data-set into n_c clusters. Cohen's Kappa [–] is defined as:

$$\text{Kappa} = \frac{\text{SSO} - S_{\text{est}}}{1 - S_{\text{est}}} \tag{13}$$

where:

$$\text{SSO} = \frac{\sum_{I=1}^{n_c} M_{I,I}}{N} \tag{14}$$

and

$$S_{\text{est}} = \frac{\sum_{I=1}^{n_c} \left[\left(\sum_{J=1}^{n_c} M_{J,I} \right) \left(\sum_{J=1}^{n_c} M_{I,J} \right) \right]}{N^2}. \tag{15}$$

N is the total sum (over rows and columns) of all the elements of **M**. Kappa ranges from −1 to 1 [–] and increases as the level of global spatial smoothness increases. Furthermore, it is a robust estimator in case of unbalanced clusters. In fact it takes into account the globally observed spatial smoothness (SSO), and also the contribution occurring by chance, namely S_{est}. Finally, the individual smoothness of each cluster C_M is quantified by means of the spatial smoothness per cluster (SS_M) index:

$$\text{SS}_M = \frac{M_{M,M}}{\sum_{I=1}^{n_c} M_{M,I}} \tag{16}$$

A simple but useful example to clarify the concepts of SS_M and spatial smoothness is reported in Appendix A.

AMTD
7, 8465–8519, 2014

4.3.3 Step 3 (Fig. 2a3)

At this stage the set of observations is divided into n_c clusters, and the spatial smoothness of this partition has been evaluated. A classical hierarchical approach would now proceed by merging the two most (data-wise) similar clusters, reducing the total number of clusters to $n_c - 1$ at each iteration.

In our case, we make additional use of the information provided by Eq. (16). Let the cluster C_W, with the lowest spatial smoothness score be defined as:

$$C_W \text{ s.t. } \quad \mathrm{SS}_W = \min_{L=1,\ldots,n_c} \mathrm{SS}_L . \tag{17}$$

The cluster C_W is forced to disappear, and it is merged with the most similar (data-wise) one according to the linkage method and the distance metric selected.

In this way, at each step of the AHC, spatial smoothness is used to identify the cluster that exhibit the highest spatial discontinuity (lowest spatial smoothness), while data similarity is used to merge it to one of the other $n_c - 1$ available clusters. The aggregative algorithm detailed in steps 1–3 recursively repeats step 2 and step 3, until $n_c = 2$. The reader should be aware that different constraints on spatial smoothness (or a direct inclusion of spatial smoothness indicators as additional dimensions of $\boldsymbol{x}^*$) could be implemented at this stage and the constraint implemented here is a specific example.

5 Selection of the optimal cluster partition

The most delicate part of any unsupervised clustering method is the selection of a partition n_{opt} that should be considered as an optimal one. This evaluation is conducted by taking into account the physical knowledge available for the process under investigation, and according to a set of cluster quality indices, that evaluate quantitatively the goodness of each possible partition (cf. Fig. 2b).

AMTD
7, 8465–8519, 2014

5.1 Cluster quality metrics

Different spatial cluster quality indices can be defined.

1. A first one is directly Kappa (Foody, 2004), defined in Eq. (13). Kappa quantifies the global degree of spatial smoothness of a given partition.

2. A second index, defined here as the accuracy spread index (AS), can be derived from Eq. (16) as follows:

$$\mathrm{AS} = \max_{L\in\{1,\ldots n_\mathrm{c}\}} \mathrm{SS}_L - \min_{L\in\{1,\ldots n_\mathrm{c}\}} \mathrm{SS}_L . \tag{18}$$

   This index evaluates the inhomogeneity of the spatial characteristics of a partition into n_c clusters. The lower this score is, the more homogeneously the n_c clusters are performing in terms of spatial scores. Lower values are therefore associated with better partitions.

Other indices can be employed to evaluate the partition from the point of view of data similarity. Most of these indices evaluate the degree of homogeneity within cluster members and the degree of heterogeneity among different clusters. In the present work we employ two indices of this kind: RMSSTD and RS (e.g. Halkidi et al., 2002a, b; Kovács and Iváncsy, 2006).

3. The root mean square standard deviation (RMSSTD) is defined as:

$$\mathrm{RMSSTD} = \sqrt{\frac{\sum_{L=1}^{n_\mathrm{c}} \sum_{k(L)=1}^{N_L} \left(\left\| \boldsymbol{x}^*_{k(L)} - \overline{\boldsymbol{x}^*}_{C_L} \right\|_2 \right)^2}{d \sum_{L=1}^{n_\mathrm{c}} (N_L - 1)}} \tag{19}$$

   where N_L is the number of objects in the Lth cluster C_L. $\boldsymbol{x}^*_{k(L)}$ and $\overline{\boldsymbol{x}^*}_{C_L}$ are the kth object and the mean value (centroid, see Eq. 6) of C_L, respectively. d is the dimensionality of $\boldsymbol{x}^*$ and $\|.\|_2$ is the 2-norm, as in Table 1. RMSSTD quantifies cluster

AMTD
7, 8465–8519, 2014

heterogeneity. Therefore good partitions (homogeneous clusters), are characterized by small RMSSTD.

4. The second data-based validity index is the *R*-squared index (RS), defined as:

$$\mathrm{RS} = \frac{\mathrm{SSQ}_t - \mathrm{SSQ}_w}{\mathrm{SSQ}_t} \tag{20}$$

where

$$\mathrm{SSQ}_w = \sum_{L=1}^{n_c} \sum_{k(L)=1}^{N_l} \left(\| \boldsymbol{x}^*_{k(L)} - \overline{\boldsymbol{x}^*}_{C_L} \|_2 \right)^2$$

$$\mathrm{SSQ}_t = \sum_{k=1}^{N} \left(\| \boldsymbol{x}^*_k - \overline{\boldsymbol{x}^*} \|_2 \right)^2$$

where SSQ_t is the total variance of the dataset (with N member objects), summed over all dimensions and SSQ_w is the average variance within each cluster. RS is therefore an index of dissimilarity between clusters and higher values indicate better clustering.

5. Eventually, a simple RKR (RMSSTD and Kappa ratio) index is defined in order to combine spatial behaviour and data similarity:

$$\mathrm{RKR} = \frac{\mathrm{RMSSTD}}{\mathrm{Kappa}} \tag{21}$$

where both indices are stretched in order to span exactly the same order of magnitudes in the interval $n_c = 1, \ldots, 1000$. The idea behind RKR is to find a trade-off between spatial smoothness (high Kappa), and data similarity (low RMSSTD). Therefore low values of RKR are associated with better partitions.

AMTD
7, 8465–8519, 2014

5.2 Evaluation

Figure 4 illustrates the behaviour of the quality indices defined as a function of the number of clusters in the dataset. Even though n_c ranges between 1 and 1000, a shorter interval is shown here, as we do not expect, given the goal of the clustering technique (i.e., hydrometeor classification), that any optimal solution would appear for very large n_c.

An optimal solution is selected here when $n_c = n_{opt} = 7$ clusters. In fact, we can observe that $n_c = 7$ corresponds to a local minimum both for AS, and RKR. This suggests that, at this level of aggregation, the spatial behaviour of each cluster is homogeneous (low AS), and the global trade-off between data similarity and spatial smoothness is optimal (local minimum RKR). Furthermore, for $n_c = 7$, Kappa is high (≈ 0.8 [–]) and RS is slightly larger than 0.5 [–]. By looking at the evolution of RS, we observe that for $n_c \leq 7$ the index tends to decrease at a higher rate. This suggests that $n_c = 7$ is an equilibrium point, where further merging of the clusters leads to high losses in terms of inter-cluster differences. Finally, we also observed that for any value $n_c < 7$, clusters related to positive Δz start to merge with clusters related to negative Δz.

6 From unlabeled clusters to hydrometeor classes

This section is devoted to the interpretation of the output of the clustering algorithm (Fig. 2c).

6.1 Global characteristics of the clusters

The seven clusters identified contain a set of observations (or objects), that have been grouped according to spatial smoothness and data similarity. These clusters are defined in the 5-dimensional space given by the dimensions of $\boldsymbol{x}^*$. A possible way to visualize the clusters is to display pairs of 2-dimensional projections of the objects $\boldsymbol{x}$.

AMTD
7, 8465–8519, 2014

Some of these projections are displayed in Fig. 5, where the seven clusters are color-coded.

Three clusters contain data collected always at positive Δz (negative temperatures), three clusters contain data collected always at negative Δz (positive temperatures) and one cluster contains mostly data collected where $\Delta z \approx 0$, even though with a larger spread. In the following, we will proceed by interpreting the clustering results separately for clusters appearing on average at $\Delta z \leq 0$ and $\Delta z > 0$.

6.2 Clusters at positive temperature

Three clusters (red, green and dark blue) in Fig. 5 are identified at positive temperatures. It is therefore assumed that they are related to liquid-phase precipitation. In order to properly associate each of them to a more specific liquid precipitation category, further analysis is performed. At first, all data classified into one of these three categories are extracted from the whole field campaign of HyMex 2012 (≈ 200 h of precipitation recorded) from PPIs taken at elevation angles ranging between 3.5° and 10°. Then, the rainfall rate R [mm h^{-1}] associated with each measurement is computed by means of the following relations (Otto and Russchenberg, 2012):

$$R = \begin{cases} 13 K_{\mathrm{dp}}^{0.75} & \text{if } Z_{\mathrm{H}} > 30\,\mathrm{dBZ} \\ \left(\frac{\zeta_{\mathrm{H}}}{243}\right)^{1/1.24} & \text{if } Z_{\mathrm{H}} \leq 30\,\mathrm{dBZ} \end{cases} \quad (22)$$

where $\zeta_{\mathrm{H}} = 10^{0.1 Z_{\mathrm{H}}}$ [mm^6 m^{-3}]. The distribution of R stratified for each class is summarized in Table 3. The green cluster is characterized by extremely low rainfall intensity, and therefore it is associated hereafter to a hydrometeor class named Drizzle (DZ). The dark blue cluster is characterized by low to intermediate rainfall intensity, and therefore it is associated to a category named light-rain (LR). Finally, the red cluster contains by far the highest rainfall intensities, and it is named hereafter heavy-rain (HR).

As an additional test, the objects contained in the 7 clusters are classified with the Hydrometeor classification scheme derived from Dolan and Rutledge (2009), hereafter

AMTD
7, 8465–8519, 2014

DR2009 (see Appendix B for the exact parametrization). The classification of the DZ, LR and HR clusters obtained with the present method is compared with the output of DR2009 in Fig. 6. Even though DR2009 does not provide three "liquid-phase" hydrometeor classes we can observe that HR is entirely classified as rain, LR is mainly classified as rain, and DZ is almost entirely associated with drizzle (in agreement with the choice made).

Figure 7 illustrates a case where DZ, LR and HR are classified on the same PPI radar image, when a high intensity convective line was approaching the radar location from the west side of the domain, leading to a layer of high values of Z_H (panel b), Z_{DR} (panel c) and K_{dp} (panel d), and to a complete extinction of the signal behind this area.

6.3 Cluster around 0 °C temperature

The yellow cluster of Fig. 5 appears on average around the 0 °C isotherm, and it is interpreted as melting snow (MS). Figure 8 shows an example of classification output, where a melting layer is clearly visible in the polarimetric observations. MS is delimiting the transition between ice-phase and liquid-phase hydrometeors, in the same way as it may be interpreted by visual inspection of the vertical stratification of Z_H (Fig. 8, panel b), Z_{DR} (panel c), and ρ_{hv} (panel e). K_{dp} (panel d) seems not to play a particular role in the classification of MS.

6.4 Clusters at negative temperatures

The clusters identified at negative temperature (dark green, pink, and light blue in Fig. 5), are more difficult to interpret and therefore more information is needed in order to associate them with an appropriate hydrometeor class. We proceed as follows: at first we examine the behaviour of the polarimetric variables within these three clusters, then we compare the classification with the output of the DR2009 algorithm, and eventually we compare the classification with the results from an in-situ based HC technique (Grazioli et al., 2014b) applied to two-dimensional video disdrometer (2DVD)

AMTD
7, 8465–8519, 2014

data, with quantitative information provided by the 2DVD itself and with the output of a numerical weather prediction model (COSMO).

6.4.1 Polarimetric signatures

Figure 9 presents the distribution of the polarimetric variables Z_H, Z_{DR}, K_{dp}, ρ_{hv}, and additionally the relative altitude Δz for the three "ice-phase" clusters.

By looking at panel a, we can observe a clear Z_H signature. Z_H takes lower values for the light-blue cluster (mode ≈ 12 dBZ), slightly higher values for the pink-cluster (mode ≈ 15 dBZ) while the dark-green cluster is characterized by the highest Z_H values (mode > 20 dBZ). This suggests that hydrometeor concentrations, size, and/or density are larger in this last cluster.

Z_{DR}, shown in panel b, exhibits a different trend. It is on average lower (but much more scattered) for the pink and light blue clusters, while slightly larger and less scattered for the dark-green one. This suggests that the light-blue and pink clusters are characterized by a higher variability of particle shapes, even though rather spherical on average (the mode of Z_{DR} is around 0.1 dB for these two clusters). The green cluster exhibits a clear mode around 0.6 dB, indicating therefore a certain degree of geometrical anisotropy. The variability of shapes of the light-blue cluster can also be observed in panel d, where it is shown that ρ_{hv} for this cluster departs often from unity.

An interesting feature is observed in panel c, where it is clear that the light-blue cluster has no K_{dp} signature (all values are close to $0^\circ\,km^{-1}$), the pink cluster is characterized by values generally lower than $1^\circ\,km^{-1}$ and the dark-green one can reach relatively large values of $2.5^\circ\,km^{-1}$. K_{dp} depends on size, concentration, shape and density of the particles in the radar resolution volume and therefore the dark green cluster contains on average more hydrometeors and/or hydrometeors of larger size and density.

AMTD
7, 8465–8519, 2014

Eventually, by looking at panel e, it can be observed that the dark-green cluster is found over a broad range of altitudes (temperatures), and that the light-blue cluster generally appears at colder temperatures than the pink one.

From this analysis, we observed that the three clusters exhibit distinct polarimetric signatures, which led us to assume the following: the light blue cluster corresponds to individual crystals and small aggregates (denoted CR), the pink cluster corresponds to aggregates (AG). Eventually, the dark green cluster corresponds to heavily rimed particles (RI). These assumptions are discussed in the following.

6.4.2 Comparison with DR2009

As a second step, DR2009 is applied to the objects classified into CR, AG and RI clusters (Fig. 10). It can be seen that, while the DR2009 "Aggregates" category is dominant both for the light blue (CR) and pink (AG) clusters, there is a larger component of vertically aligned ice (a type of small crystals) in the light-blue cluster, as well as a large component of crystals. The dark green cluster is split between aggregates (≈ 15 %), vertically aligned ice (≈ 15 %) and rimed particles (HDG + LDG ≈ 70 %). These observations are in agreement with the previous assumptions.

6.4.3 Comparison with 2DVD classification output

An additional comparison is conducted with the output of a HC scheme developed for two-dimensional video disdrometers (2DVD, e.g. Kruger and Krajewski, 2002, for more information on the instrument). This method, hereafter called HC-2DVD is described in Grazioli et al. (2014b).

HC-2DVD is applied to the two-dimensional images collected by a 2DVD, and it provides an estimate of the dominant category of hydrometeor that was recorded by the instrument over time intervals of 60 s. Thus the classification is conducted spatially at the point-scale (disdrometer measurement), but it is averaged in time. HC-2DVD discriminates between eight hydrometeor classes: Small particle-like (SP), Dendrite-like (D),

AMTD
7, 8465–8519, 2014

Column-like (C), Graupel-like (G), Rimed particle-like (RIM), Aggregate-like (AG), Melting snow-like (MS), and Rain (R). The "-like" is added to underline that this approach identifies the dominant type of hydrometeor, and that there is in general a mixture of different hydrometeors that do not necessarily exhibit the pristine shape.

Here we compare HC-2DVD with the output of the clustering algorithm over all the snowfall events collected during the campaign of Davos 2009–2011 (Sect. 3). As observed in Fig. 1a, one 2DVD was located, during the campaign, at a projected distance of about 5.2 km from the location of MXPol. The PPI of lowest elevation and not contaminated by clutter was taken at 9° elevation with a repetition interval of five minutes. This PPI is used to compare with HC-2DVD.

Before discussing the comparison it must be kept in mind that: (i) the closest radar resolution volume center was about 400 m above the 2DVD (the spatial match is not perfect), (ii) the sampling times and volumes of the two instruments are different. Therefore this comparison is rather qualitative.

The comparison is conducted on a subset of about 30 snowfall events selected by means of visual inspection. The events with large temporal and spatial variability or poor/suspicious data quality are removed from the analysis, in order to avoid additional uncertainties in the comparison. Radar resolution volumes situated within 150 m in horizontal distance from the 2DVD location are selected and compared with the HC-2DVD output and a buffer of ±2 min is applied in order to match multiple 2DVD observations with a single radar scan.

Figure 11 presents the results obtained. We can observe that the characteristics of the CR (light-blue) and AG (pink) clusters are similar. The main difference is that HC-2DVD tends to associate slightly more small particles, dendrites and graupel to CR, and slightly more aggregates to AG. Interestingly, the RI (dark-green) cluster is mainly associated by HC-2DVD to aggregates, rimed particles and columns. Furthermore RI, among these three clusters, has the lowest component in terms of small particles.

The large presence of columns in the RI cluster is not in contrast with the assumption of rimed particles. In fact, solid columns and needles in particular, are produced

AMTD
7, 8465–8519, 2014

in temperature ranges overlapping the ones at which rimed particles are frequently observed. Needles are produced efficiently around −5 °C, and solid columns between −5 °C and −10 °C, while rimed particles can be observed from slightly positive temperatures until −20 °C (Pruppacher and Klett, 1997; Dolan and Rutledge, 2009). Finally, the dominance of aggregates in the RI cluster in Fig. 11 can be explained by the presence of large aggregates undergoing the early stages of riming (whose shape is not yet smooth enough to be classified as rimed particles or graupel by HC-2DVD).

6.4.4 Comparison with 2DVD in terms of snowfall intensity

Additionally to the qualitative information provided by HC-2DVD, the 2DVD observations can be used in a quantitative way to investigate the relation between the content of the three clusters and the intensity of snowfall. Here we quantify the snowfall intensity by means of an equivalent flux (EF), defined as:

$$\mathrm{EF} = \frac{4\pi \sum_{i=1}^{N(\Delta t)} \mathrm{De}_i^3}{3\Delta t\, A} \tag{23}$$

where Δt is the temporal resolution at which EF is calculated (1/60 h here), A is the measurement area of the instrument [mm^2], $N(\Delta t)$ is the number of particles recorded in Δt, and De_i the equivalent diameter of a snowflake [mm], as defined in Huang et al. (2010). Given the assumptions in the estimation of De, EF can be erroneous in absolute terms and therefore it is used here to compare the content of the three clusters in relative terms only. Figure 12 shows the distribution of EF for the three clusters (CR, AG, RI). It can be seen that the snowfall intensity differs among these three. CR exhibits the lowest intensities, AG intermediate ones, and RI the highest intensities. This is the expected behavior of rimed particles, characterized by larger densities and therefore larger fall velocities and EF.

AMTD
7, 8465–8519, 2014

Summarizing the interpretation conducted until now, the cluster CR is composed mainly of individual crystal and small aggregates, AG is associated with aggregates, while RI is considered as an indicator of riming.

6.4.5 CR, AG, RI: classification example

Figure 13 presents an example of ice-phase precipitation. The temperature at the location of MXPol ($y = 0$, $x = 0$ in the figure), was about $-5\,^{\circ}$C at the selected time-step. In panel a it can be observed a stratification of the precipitation into three layers. At higher altitudes (> 4 km above radar location) there is a thin layer classified mostly as crystals (CR). The crystals turn into aggregates (AG), that dominates the precipitation in a second layer (between 3.5 and 4 km above MXPol), and finally (below 3.5 km above MXPol) RI dominates the precipitation. RI is characterized by larger values of K_{dp} (up to $2^{\circ}\,km^{-1}$) and Z_H (up to 25 dBZ). CR instead is characterized by low values of Z_H and ρ_{hv} (as low as 0.9 [–]), and very low values of K_{dp}. AG in this example exhibits polarimetric signatures somehow intermediate between CR and RI.

For illustrative purpose, the situation corresponding to Fig. 13 was simulated using the numerical weather model COSMO (see online at http://www.cosmo-model.org). The model, operationally used by MeteoSwiss, was run at about 2 km resolution with forcing from MeteoSwiss reanalysis. As shown in Fig. 14, COSMO predicts the presence of supercooled liquid water (QC) at the higher altitudes, and graupel (QG) mixed with snow (QS) below it. Both the presence of supercooled liquid water in the clouds, and the explicit presence of graupel in precipitation are in agreement with the layer of rimed particles RI classified in Fig. 13a.

7 Summary and conclusions

A novel approach to hydrometeor classification from polarimeteric weather radar was presented in this manuscript. The method is applied to a dataset of radar data collected

AMTD
7, 8465–8519, 2014

by an X-band polarimetric radar. The approach is not based on numerical scattering simulations, and the number and type of hydrometeor classes is not defined a-priori.

The available amount of polarimetric observations is reduced to a representative subset. This subset undergoes a hierarchical clustering algorithm with spatial constraints, that groups similar observations according to both the (data-driven) similarity and the spatial smoothness of each partition. This means that we made the assumption of smooth spatial transitions between hydrometeor types. Following this strategy, an optimal number of 7 clusters is found. Three clusters are found at positive temperatures and they are interpreted as drizzle (DZ), light rain (LR) and heavy rain (HR), according to the rainfall rate associated with them (and according to the comparison with the algorithm DR2009, for verification purposes). One cluster appears systematically around 0 °C temperatures and is associated with melting snow (MS). Finally, three clusters are found at negative temperatures and they are interpreted as (dominated by) crystals/small aggregates (CR), aggregates (AG) and rimed particles (RI).

The proposed approach is the first attempt, using unsupervised classification, to move the starting point of a classification algorithm away from scattering simulations conducted over an arbitrarily defined number of hydrometeor classes to the identification of relevant clusters in the data themselves.

Among the advantages of the approach, we remind that it is independent from systematic biases that may affect the polarimetric observations, and the data-driven approach ensures that the identified clusters take into account the accuracy of the instrument. Finally, the method is adaptable to other radar systems and can be tuned to include other constraints about the spatial smoothness of the partition or temporal consistency. The main limitations of the method are related to the interpretation of the content of the clusters, that might not be trivial especially if no ground reference is available for comparison. Additionally, the method is as representative as the available data-base is, and the clusters identified are a-priori valid only for the instrument employed to collect the data. We nevertheless expect the number of clusters to be very similar for similar radar systems and datasets.

AMTD
7, 8465–8519, 2014

It is interesting to note that the method exploits the hypotesis of spatial smoothness of the hydrometeor classes only in general terms, when the full data-base of observation is hierarchically clustered. Future work could be devoted to extend the constraints involving spatial smoothness also to newly classified images, once the clusters have been already defined and interpreted or to include the spatial information directly in the distance metric of the clustering process. Also, this clustering approach (or some steps of the approach) could be employed as a support to fuzzy-logic based classification methods, to improve or adapt the membership functions according to the clustering outputs, in specific datasets.

Appendix A: Spatial smoothness evaluation: a visual example

In this section, we provide a visual example for the interpretation of the SS_M index presented in Sect. 4.3.2. Let us consider the situation of Fig. A1, that represents a simplified and hypothetical partition of three clusters in a limited physical space of 5×5 pixels.

It is evident that clusters C_1 and C_2 are the most spatially coherent, while C_3 is spatially discontinuous. This is reflected in their spatial scores. In fact $SS_1 = 0.68$ [–], $SS_2 = 0.63$ [–] and $SS_3 = 0$ [–]. Therefore, referring to Fig. 2a and step 3, the cluster C_3 will be forced to merge with the one which is most similar to it (data-wise), either C_1 or C_2, leading to a new partition into only 2 clusters with a better spatial score.

However, it must be underlined that: (i) this is only a very simple and spatially limited example (i.e., the edges here have an impact on the results), (ii) the actual geometry of neighbouring radar observations (defined in polar coordinates) is not the one depicted in this example, but the one shown in Fig. 3.

Appendix B: DR2009 algorithm

The algorithm denoted as DR2009 in this paper is based on the work of Dolan and Rutledge (2009), with some adaptations. In this Appendix, we provide the exact

AMTD
7, 8465–8519, 2014

parametrization of the membership functions for the fuzzy-logic scheme, as well as the weights assigned to each polarimetric variable. The input variables of the algorithm are Z_H [dBZ], Z_{DR} [dB], K_{dp} [° km^{-1}], ρ_{hv} [–] and Δz [m] and their weights in the fuzzy logic scheme are 0.25, 0.25, 0.25, 0.08 and 0.17, respectively. The hydrometeor classes available are aggregates (AG), crystals (CR), drizzle (DZ), high density graupel (HDG), low density graupel (LDG), rain (R), vertical ice (VI) and wet snow (WS, not present in Dolan and Rutledge, 2009). The membership function employed for all the polarimetric inputs is a membership beta function β, while for Δz a trapezoidal one is used. β is defined as:

$$\beta = \frac{1}{1 + \left(\frac{x-m}{a}\right)^{2b}} \tag{B1}$$

where x is the considered polarimetric variable, m is the midpoint, a is the width and b the slope. Table 4 summarizes the values of the parameters for each polarimetric variable and each hydrometeor class.

The trapezoidal membership function T employed for Δz takes instead the form of:

$$T = \begin{cases} 0 & \text{if } x < l_1; \\ \frac{x-l_1}{l_2-l_1} & \text{if } l_1 < x \le l_2; \\ 1 & \text{if } l_2 < x \le r_1; \\ \frac{r_2-x}{r_2-r_1} & \text{if } r_1 < x \le r_2; \\ 0 & \text{if } x > r_2 \end{cases} \tag{B2}$$

where l_1, l_2, r_1 and r_2 define the four vertices of the trapezoid. The values for these parameters are reported in Table 5.

Acknowledgements. This work is a contribution to the HyMeX programme. The authors acknowledge Météo-France for supplying temperature data and the HyMeX database teams (ESPRI/IPSL and SEDOO/Observatoire Midi-Pyrénées) for their help in accessing the data. The

AMTD
7, 8465–8519, 2014

authors are also thankful to all the members of EPFL-LTE that were involved during the field campaigns in the deployment and maintenance of the instruments, and later in the processing of the data. The work was supported by the Swiss National Science Foundation under grant 136827. The authors are also thankful to Daniel Wolfensberger (EPFL-LTE) for the COSMO2 reanalysis of Sect. 6.4.5.

References

Al-Sakka, H., Boumahmoud, A.-A., Fradon, B., Frasier, S. J., and Tabary, P.: A new fuzzy logic hydrometeor classification scheme applied to the French X-, C-, and S-band polarimetric radars, J. Appl. Meteorol. Clim., 52, 2328–2344, doi:10.1175/JAMC-D-12-0236.1, 2013. 8467

Bechini, R., Baldini, L., and Chandrasekar, V.: Polarimetric Radar Observations in the Ice Region of Precipitating Clouds at C-Band and X-Band Radar Frequencies, J. Appl. Meteorol. Clim., 52, 1147–1169, doi:10.1175/JAMC-D-12-055.1, 2013. 8467

Berne, A. and Krajewski, W. F.: Radar for hydrology: Unfulfilled promise or unrecognized potential?, Adv. Water Resour., 51, 357–366, doi:10.1016/j.advwatres.2012.05.005, 2013. 8467

Bousquet, O., Berne, A., Delanoë, J., Dufournet, Y., Gourley, J. J., Van-Baelen, J., Augros, C., Besson, L., Boudevillain, B., Caumont, O., Defer, E., Grazioli, J., Jorgensen, D. J., Kirstetter, P.-E., Ribaud, J.-F., Beck, J., Delrieu, G., Ducrocq, V., Scipion, D., Schwarzenboeck, A., and Zwiebel, J.: Multiple-frequency radar observations collected in southern france during the field phase of the hydrometeorological cycle in the mediterranean experiment (HyMeX), B. Am. Meteorol. Soc., online first, doi:10.1175/BAMS-D-13-00076.1, 2014. 8473

Bringi, V. N. and Chandrasekar, V.: Polarimetric Doppler Weather Radar, Cambridge University Press, 2001. 8467

Chandrasekar, V., Keranen, R., Lim, S., and Moisseev, D.: Recent advances in classification of observations from dual polarization weather radars, Atmos. Res., 119, 97–111, doi:10.1016/j.atmosres.2011.08.014, 2013. 8467

Dolan, B. and Rutledge, S. A.: A theory-based hydrometeor identification algorithm for X-band polarimetric radars, J. Atmos. Ocean. Tech., 26, 2071–2088, doi:10.1175/2009JTECHA1208.1, 2009. 8467, 8475, 8485, 8490, 8493, 8494

AMTD
7, 8465–8519, 2014

Dolan, B., Rutledge, S. A., Lim, S., Chandrasekar, V., and Thurai, M.: A robust C-band hydrometeor identification algorithm and application to a long-term polarimetric radar dataset, J. Appl. Meteorol. Clim., 52, 2162–2186, doi:10.1175/JAMC-D-12-0275.1, 2013. 8467

Foody, G. M.: Thematic map comparison: evaluating the statistical significance of differences in classification accuracy, Photogramm. Eng. Rem. S., 50, 627–633, 2004. 8482

Gourley, J. J., Tabary, P., and Parent-du Chatelet, J.: A fuzzy logic algorithm for the separation of precipitating from nonprecipitating echoes using polarimetric radar observations, J. Atmos. Ocean. Tech., 24, 1439–1451, doi:10.1175/JTECH2035.1, 2007. 8467

Grazioli, J., Schneebeli, M., and Berne, A.: Accuracy of phase-based algorithms for the estimation of the specific differential phase shift using simulated polarimetric weather radar data, IEEE Geosci. Remote S., 11, 763–767, doi:10.1109/LGRS.2013.2278620, 2014a. 8475

Grazioli, J., Tuia, D., Monhart, S., Schneebeli, M., Raupach, T., and Berne, A.: Hydrometor classification from 2 dimensional videodisdrometer data, Atmos. Meas. Tech. Discuss., 7, 1603–1644, doi:10.5194/amtd-7-1603-2014, 2014b. 8486, 8488

Halkidi, M., Batistakis, Y., and Vazirgiannis, M.: Cluster validity methods: Part I, SIGMOD Record, 31, 40–45, 2002a. 8482

Halkidi, M., Batistakis, Y., and Vazirgiannis, M.: Clustering validity checking methods: Part II, SIGMOD Record, 31, 19–27, 2002b. 8482

Huang, G., Bringi, V. N., Cifelli, R., Hudak, D., and Petersen, W. A.: A methodology to derive radar reflectivity liquid equivalent snow rate relations using C-band radar and a 2D video disdrometer, J. Atmos. Ocean. Tech., 27, 637–651, 2010. 8490

Jain, A. K. and Dubes, R. C.: Algorithms for Clustering Data, Prentice-Hall, Inc., Upper Saddle River, NJ, USA, 1988. 8470

Jain, A. K., Murty, M. N., and Flynn, P. J.: Data clustering: a review, ACM Comput. Surv., 31, 264–323, 1999. 8468

Jain, A. K., Duin, R. P. W., and Mao, J. C.: Statistical pattern recognition: a review, IEEE T. Pattern Anal., 22, 4–37, doi:10.1109/34.824819, 2000. 8469

Jameson, A. R.: Microphysical interpretation of multi-parameter radar measurements in rain: Part II: estimation of raindrop distribution parameters by combined dual-wavelength and polarization measurements, J. Atmos. Sci., 40, 1803–1813, 1983. 8467

Kovács, F., and Iváncsy, R.: Cluster Validity Measurement for Arbitrary Shaped Clusters, in: Proceedings of the 5th WSEAS International Conference on Artificial Intelligence, Knowl-

AMTD
7, 8465–8519, 2014

edge Engineering and Data Bases, World Scientific and Engineering Academy and Society (WSEAS), Madrid, Spain, 372–377, 2006. 8472, 8482
Kruger, A. and Krajewski, W. F.: Two-dimensional video disdrometer: a description, J. Atmos. Ocean. Tech., 19, 602–617, 2002. 8488
Liu, H. P. and Chandrasekar, V.: Classification of hydrometeors based on polarimetric radar measurements: Development of fuzzy logic and neuro-fuzzy systems, and in situ verification, J. Atmos. Ocean. Tech., 17, 140–164, 2000. 8467
Marzano, F., Scaranari, D., and Vulpiani, G.: Supervised fuzzy-logic classification of hydrometeors using C-band weather radars, IEEE T. Geosci. Remote, 45, 3784–3799, doi:10.1109/TGRS.2007.903399, 2007. 8467
Marzano, F. S., Botta, G., and Montopoli, M.: Iterative Bayesian retrieval of hydrometeor content from X-band polarimetric weather radar, IEEE T. Geosci. Remote, 48, 3059–3074, 2010. 8467
Mishchenko, M. I., Travis, L. D., and Mackowski, D. W.: T-matrix computations of light scattering by nonspherical particles: a review, J. Quant. Spectrosc. Ra., 55, 535–575, 1996. 8468
Muth, X., Schneebeli, M., and Berne, A.: A sun-tracking method to improve the pointing accuracy of weather radar, Atmos. Meas. Tech., 5, 547–555, doi:10.5194/amt-5-547-2012, 2012. 8472
Otto, T. and Russchenberg, H. W. J.: Estimation of specific differential phase and differential backscatter phase from polarimetric weather radar measurements of rain, IEEE Geosci. Remote S., 8, 988–992, doi:10.1109/LGRS.2011.2145354, 2011. 8475
Otto, T. and Russchenberg, H. W. J.: Rainfall rate retrieval with IDRA, the polarimetric X-band radar at Cabauw, Netherlands., in: Proc. ERAD 2012 – The seventh European conference on radar in meteorology and hydrology, Toulouse, FR, 2012. 8475, 8485
Pruppacher, H. R. and Klett, R. L.: Microphysics of Clouds and Precipitation, no. 18 in Atmospheric and Oceanographic Sciences Library, 2nd edn., Kluwer Academic Press, 1997. 8490
Ryzhkov, A. V., Schuur, T. J., Burgess, D. W., Heinselman, P. L., Giangrande, S. E., and Zrnic, D. S.: The joint polarization experiment, polarimetric rainfall measurements and hydrometeor classification, B. Am. Meteorol. Soc., 86, 809–824, doi:10.1175/BAMS-86-6-809, 2005. 8467

AMTD
7, 8465–8519, 2014

Schleiss, M., Jaffrain, J., and Berne, A.: Stochastic simulation of intermittent DSD fields in time, J. Hydrometeorol., 13, 621–637, doi:10.1175/JHM-D-11-018.1, 2012. 8473
Schneebeli, M., Dawes, N., Lehning, M., and Berne, A.: High-resolution vertical profiles of polarimetric X-band weather radar observables during snowfall in the Swiss Alps, J. Appl. Meteorol. Clim., 52, 378–394, doi:10.1175/JAMC-D-12-015.1, 2013. 8467
Schneebeli, M., Grazioli, J., and Berne, A.: Improved estimation of the specific differential phase shift using a compilation of Kalman filter ensembles, IEEE T. Geosci. Remote, 52, 5137–5149, doi:10.1109/TGRS.2013.2287017, 2014. 8473
Scipion, D., Mott, R., Lehning, M., Schneebeli, M., and Berne, A.: Seasonal small-scale spatial variability in alpine snowfall and snow accumulation, Water Resour. Res., 49, 1446–1457, doi:10.1002/wrcr.20135, 2013. 8501
Seliga, T. A. and Bringi, V. N.: Potential use of differential reflectivity measurements at orthogonal polarizations for measuring precipitation, J. Appl. Meteorol., 15, 69–76, 1976. 8467
Snyder, J. C., Bluestein, H. B., Zhang, G., and Frasier, S. J.: Attenuation correction and hydrometeor classification of high-resolution, X-band, dual-polarized mobile measurements in severe convective storms, J. Atmos. Ocean. Tech., 27, 1979–2001, doi:10.1175/2010JTECHA1356.1, 2010. 8467
Straka, J. M., Zrnic, D. S., and Ryzhkov, A. V.: Bulk hydrometeor classification and quantification using polarimetric radar data: synthesis of relations, J. Appl. Meteorol., 39, 1341–1372, 2000. 8467
Testud, J., Le Bouar, E., Obligis, E., and Ali-Mehenni, M.: The rain profiling algorithm applied to polarimetric weather radar, J. Atmos. Ocean. Tech., 17, 332–356, 2000. 8473
Tyynela, J., Leinonen, J., Moisseev, D., and Nousiainen, T.: Radar backscattering from snowflakes: comparison of fractal, aggregate, and soft spheroid models, J. Atmos. Ocean. Tech., 28, 1365–1372, doi:10.1175/JTECH-D-11-00004.1, 2011. 8468
Vivekanandan, J., Bringi, V. N., Hagen, M., and Meischner, P.: Polarimetric radar studies of atmospheric ice particles, IEEE T. Geosci. Remote, 32, 1–10, 1994. 8467
Volpi, M., Tuia, D., and Kanevski, M.: Memory-based cluster sampling for remote sensing image classification, IEEE T. Geosci. Remote, 50, 3096–3106, 2012. 8477
Von Luxburg, U.: A tutorial on spectral clustering, Stat. Comput., 17, 395–416, 2007. 8468
Ward, J.: Hierarchical grouping to optimize an objective function, J. Am. Stat. Assoc., 58, 236–244, 1963. 8469

AMTD
7, 8465–8519, 2014

Wilks, D. S. (Ed.): Statistical Methods in the Atmospheric Sciences, Vol. 100 of International Geophysics, Academic Press, 2011. 8472, 8475, 8479

Xu, R. and Wunsch, D.: Survey of clustering algorithms, IEEE T. Neural Networ., 16, 645–678, doi:10.1109/TNN.2005.845141, 2005. 8468, 8469

AMTD

7, 8465–8519, 2014

Table 1. Example of commonly used distance metrics $D(\boldsymbol{x}, \boldsymbol{y})$. The notation $\|\boldsymbol{x}\|_p$ refers to the p-norm of $\boldsymbol{x}$: $\|\boldsymbol{x}\|_p = \left(\sum_{i=1}^{d} |\boldsymbol{x}[i]|^p\right)^{1/p}$.

$D(\boldsymbol{x}, \boldsymbol{y})$	Expression	Definitions
Minkowksi	$\|\boldsymbol{x} - \boldsymbol{y}\|_p$	p: free parameter
Superior	$\max_{i=1,\ldots,d} \|\boldsymbol{x}[i] - \boldsymbol{y}[i]\|$	–
Cosine	$\frac{\boldsymbol{x}^{\mathsf{T}}\boldsymbol{y}}{\|\boldsymbol{x}\|_1 \|\boldsymbol{y}\|_1}$	$^{\mathsf{T}}$: transpose
Correlative	$\sqrt{\frac{1-r(\boldsymbol{x},\boldsymbol{y})}{2}}$	r: Pearson correlation coefficient

AMTD
7, 8465–8519, 2014

Table 2. Main characteristic of the X-band polarimetric weather radar MXPol. Additional information on the instrument can be found in Scipion et al. (2013).

Parameter	Value
Radar Type	Pulsed
Frequency	9.41 [GHz]
Polarization	H-V hortogonal
Transmission/Reception	Simultaneous (STAR)
3 dB beamwidth	1.45 [°]
Max. range	30–35 [km]
Range resolution	75 [m]

AMTD
7, 8465–8519, 2014

Table 3. Rainfall rate R [mm h^{-1}] associated with the three clusters appearing at positive temperatures. Some relevant quantiles (Q5, Q25, Q50, Q75, Q95) of the full distribution are given here.

Cluster	Q5	Q25	Q50	Q75	Q95
Green	0.01	0.04	0.12	0.25	2.5
Dark blue	0.1	2.15	4.8	7.5	15
Red	4.3	12	22	32	57

AMTD
7, 8465–8519, 2014

Table 4. Parametrization of the membership beta functions β employed in the DR2009 algorithm.

Variable	class	a	m	b
Z_H	Aggregates (AG)	17.0	16.0	3.0
Z_{DR}	Aggregates (AG)	0.7	0.7	3.0
K_{dp}	Aggregates (AG)	0.2	0.2	2.0
ρ_{hv}	Aggregates (AG)	0.011	0.989	1.0
Z_H	Crystals (CR)	22.0	−3.0	3.0
Z_{DR}	Crystals (CR)	2.6	3.2	3.0
K_{dp}	Crystals (CR)	0.15	0.15	2.0
ρ_{hv}	Crystals (CR)	0.015	0.985	1.0
Z_H	Drizzle (DZ)	29.0	2.0	3.0
Z_{DR}	Drizzle (DZ)	0.5	0.5	3.0
K_{dp}	Drizzle (DZ)	0.18	0.18	2.0
ρ_{hv}	Drizzle (DZ)	0.007	0.992	1.0
Z_H	High density graupel (HDG)	11.0	43.0	3.0
Z_{DR}	High density graupel (HDG)	2.5	1.2	3.0
K_{dp}	High density graupel (HDG)	5.1	2.5	2.0
ρ_{hv}	High density graupel (HDG)	0.018	0.983	1.0
Z_H	Low density graupel (LDG)	10.0	34.0	3.0
Z_{DR}	Low density graupel (LDG)	1.0	0.3	3.0
K_{dp}	Low density graupel (LDG)	2.1	0.7	2.0
ρ_{hv}	Low density graupel (LDG)	0.007	0.993	1.0
Z_H	Rain (R)	17.0	42.0	3.0
Z_{DR}	Rain (R)	2.8	2.7	3.0
K_{dp}	Rain (R)	12.9	12.6	2.0
ρ_{hv}	Rain (R)	0.01	0.99	1.0
Z_H	Vertical ice (VI)	28.5	3.5	3.0
Z_{DR}	Vertical ice (VI)	1.3	−0.8	3.0
K_{dp}	Vertical ice (VI)	0.08	−0.1	2.0
ρ_{hv}	Vertical ice (VI)	0.035	0.965	1.0
Z_H	Wet snow (WS)	20.0	30.0	3.0
Z_{DR}	Wet snow (WS)	1.4	2.2	3.0
K_{dp}	Wet snow (WS)	1.0	1.0	2.0
ρ_{hv}	Wet snow (WS)	0.135	0.835	1.0

AMTD
7, 8465–8519, 2014

Table 5. Parametrization of the trapezoidal membership function T employed for the non polarimetric variable Δz [m].

Variable	class	l_1	l_2	r_1	r_2
Δz	Aggregates (AG)	0	500	20 000	25 000
Δz	Crystals (CR)	0	500	20 000	25 000
Δz	Drizzle (DZ)	−25 000	−20 000	−100	0
Δz	High density graupel (HDG)	−600	100	20 000	25 000
Δz	Low density graupel (LDG)	−600	100	20 000	25 000
Δz	Rain (R)	−25 000	−20 000	−100	0
Δz	Vertical ice (VI)	−50	0	20 000	25 000
Δz	Wet snow (WS)	−1000	−700	700	1000

AMTD
7, 8465–8519, 2014

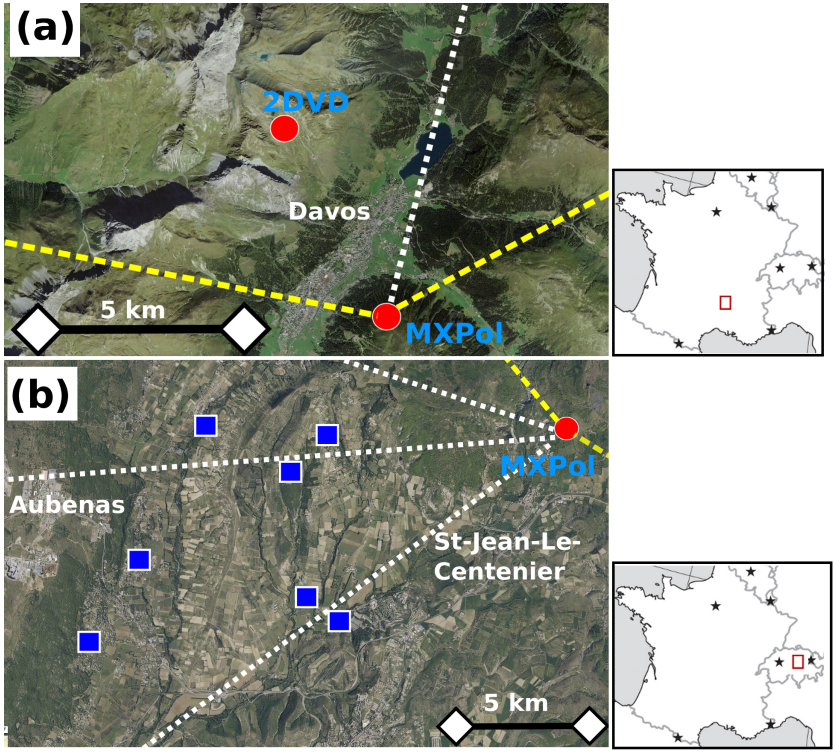

Figure 1. Maps of the two field deployments of MXPol considered in this study. **(a)** Deployment in Davos (CH), **(b)** deployment in Montbrun (FR). The yellow lines indicates the extent of the PPI sector scans, while the white lines indicates the directions of the RHI scans. Red circles are used to mark the locations of instruments directly employed in the study, while blue squares are used for Parsivel-type disdrometers (employed only to parametrize polarimetric power laws). The source of the aerial view of **(a)** is http://www.geo.admin.ch, and of **(b)** is http://www.geoportail.gouv.fr/.

AMTD
7, 8465–8519, 2014

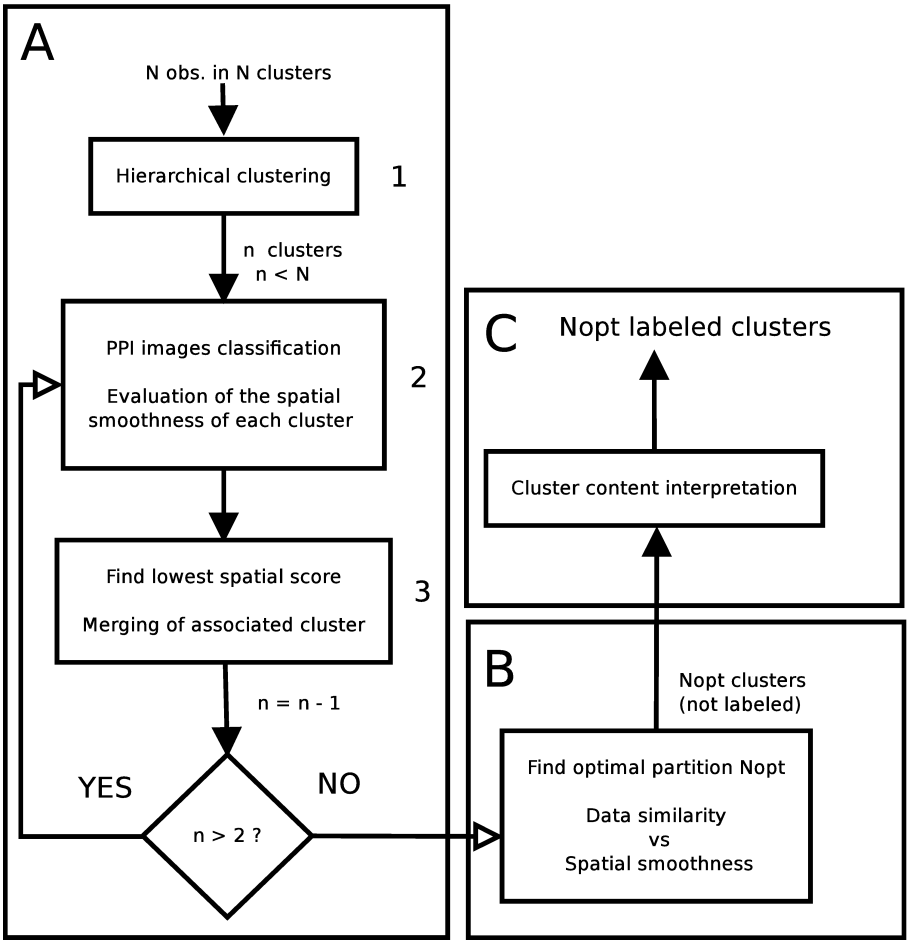

Figure 2. Flow chart of the clustering algorithm presented in Sect. 4.

AMTD
7, 8465–8519, 2014

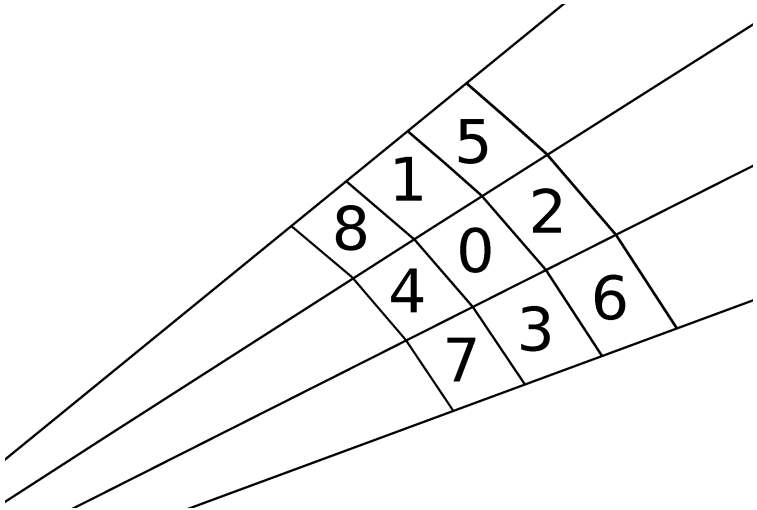

Figure 3. Schematic representation of the position of the 8 nearest neighbours of the radar resolution volume labeled with the number 0.

AMTD
7, 8465–8519, 2014

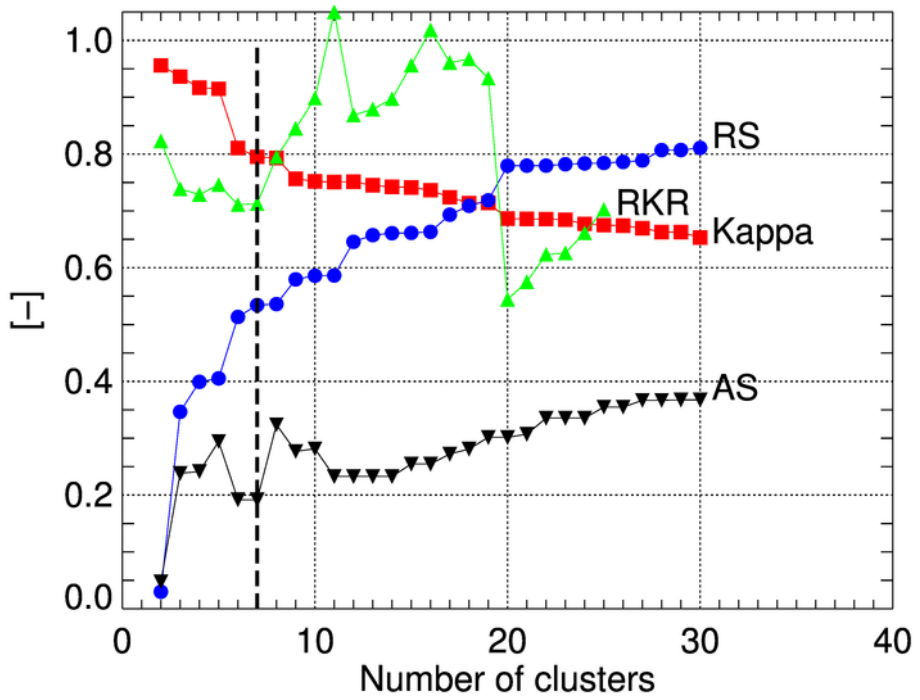

Figure 4. Evolution of Kappa, RKR, RS and AS as a function of the number of clusters in the data-set. The vertical line at $n_c = 7$ shows the selected final number of clusters.

AMTD
7, 8465–8519, 2014

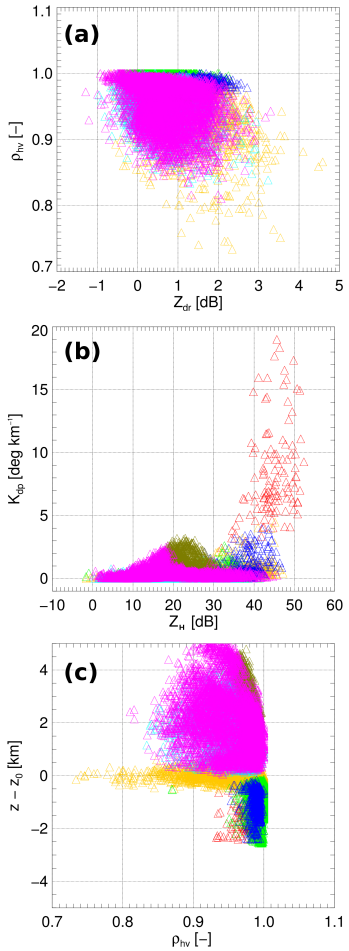

Figure 5. Three examples of 2-D projection of the 7 clusters found in the dataset. Different colors refer to different clusters. **(a)**: Z_{DR} vs. ρ_{hv}, **(b)**: Z_H vs. K_{dp}, **(c)**: Δz vs. ρ_{hv}.

AMTD
7, 8465–8519, 2014

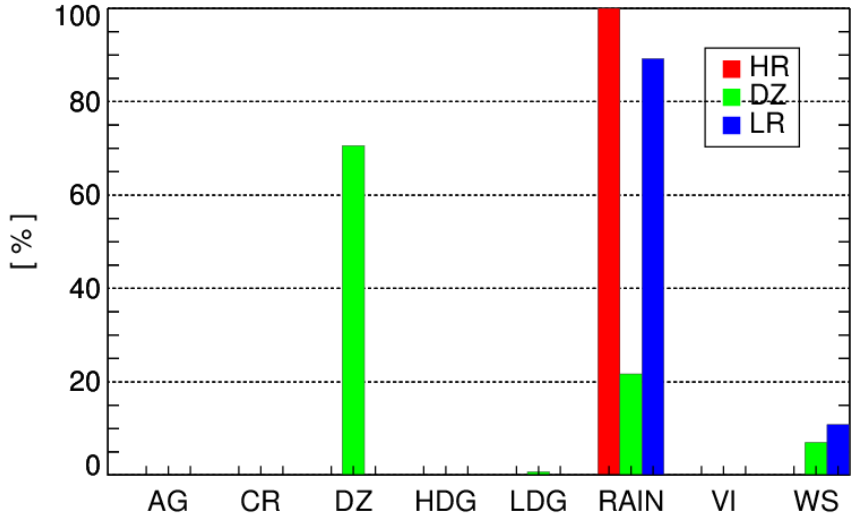

cc

Figure 6. Classification output of the DR2009 HC method applied to the three clusters appearing at positive temperatures. On the x-axis are indicated the categories from DR2009 and on the y-axis the proportion of cluster members belonging to a given category. All the bars of the same color sum up to one.

AMTD
7, 8465–8519, 2014

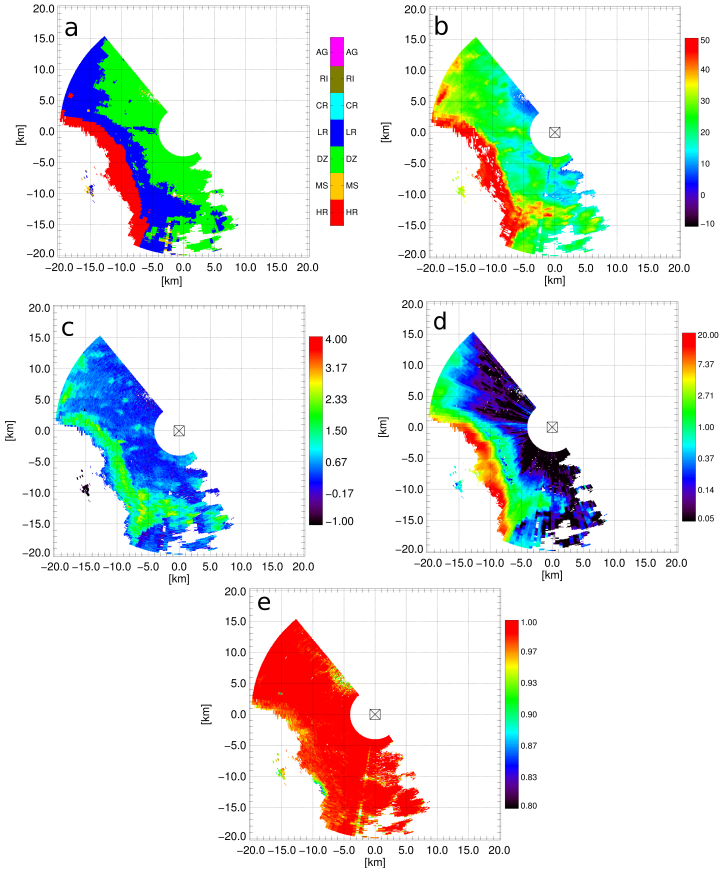

Figure 7. Hydrometeor classification and polarimetric observation from a PPI sector scan collected the 24 September during HyMeX SOP 2012 at 02:12 UTC with an elevation angle of 3.5°. **(a)** Hydrometeor classification with the clustering approach, **(b)** Z_H [dBZ], **(c)** Z_{DR} [dB], **(d)** K_{dp} [° km^{-1}], **(e)** ρ_{hv} [–]. The spatial coordinates originates at the radar location.

AMTD
7, 8465–8519, 2014

Hydrometeor classification from polarimetric radar measurements: a clustering approach

J. Grazioli et al.

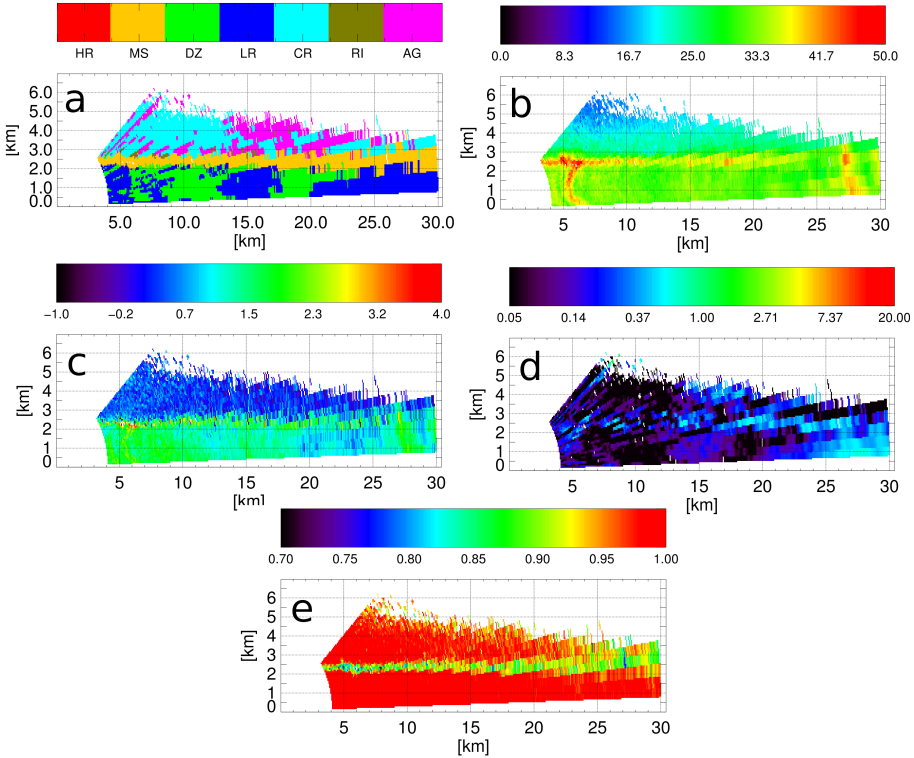

Figure 8. Hydrometeor classification and polarimetric observation from an RHI collected the 29 September during HyMeX SOP 2012 at 13:28 UTC. **(a)** Hydrometeor classification with the clustering approach, **(b)** Z_H [dBZ], **(c)** Z_{DR} [dB], **(d)** K_{dp} [$^\circ$ km^{-1}], **(e)** ρ_{hv} [–]. The spatial coordinates originate at the radar location (the altitude of the radar is 605 m).

AMTD
7, 8465–8519, 2014

Hydrometeor classification from polarimetric radar measurements: a clustering approach

J. Grazioli et al.

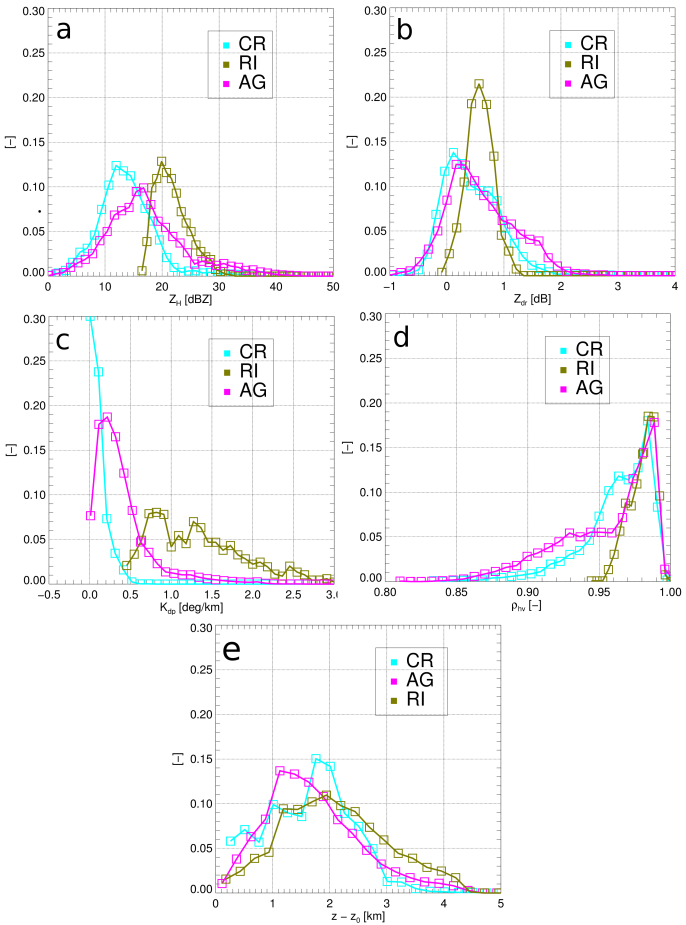

Figure 9. Distribution within the three clusters found in the ice-phase of: **(a)** Z_H [dBZ], **(b)** Z_{DR} [dB], **(c)** K_{dp} [° km^{-1}], **(d)** ρ_{hv} [–], **(e)** Δz [km].

AMTD
7, 8465–8519, 2014

Hydrometeor classification from polarimetric radar measurements: a clustering approach

J. Grazioli et al.

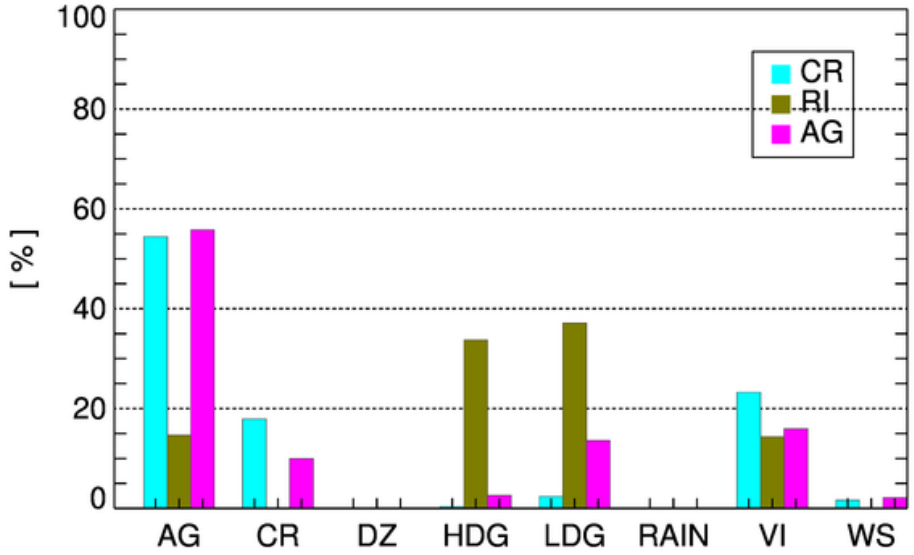

Figure 10. As in Fig. 6, for the three clusters identified at freezing temperatures.

AMTD
7, 8465–8519, 2014

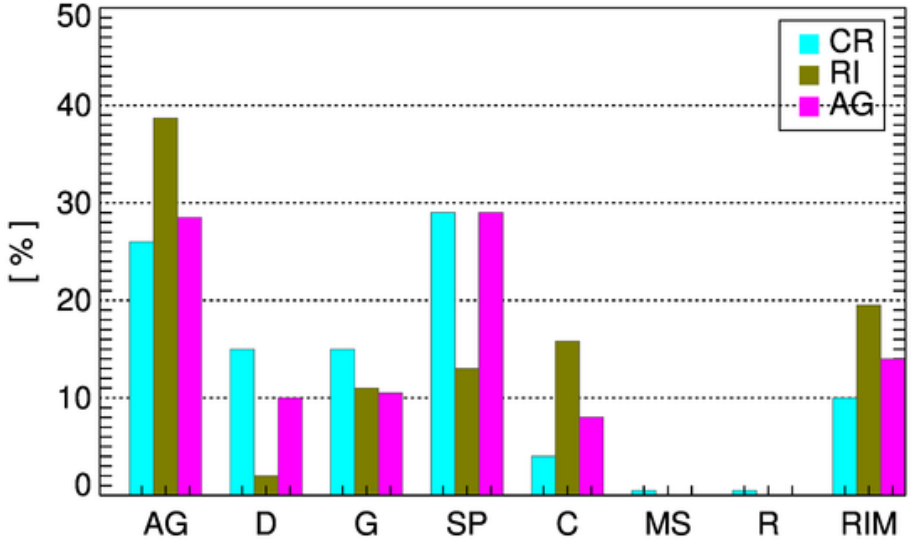

Figure 11. As in Fig. 6, for the three clusters identified at freezing temperatures and referring to the comparison with HC-2DVD.

AMTD
7, 8465–8519, 2014

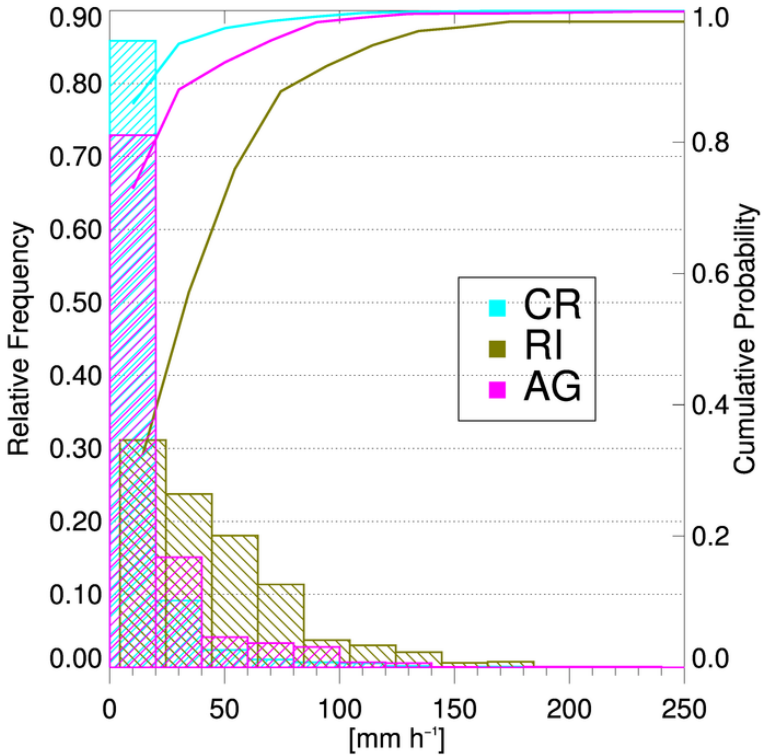

Figure 12. Histogram density and cumulative density of snowfall intensity, as quantified by the equivalent flux EF [mm h^{-1}], measured by the 2DVD and associated with the three clusters identified at freezing temperatures.

AMTD
7, 8465–8519, 2014

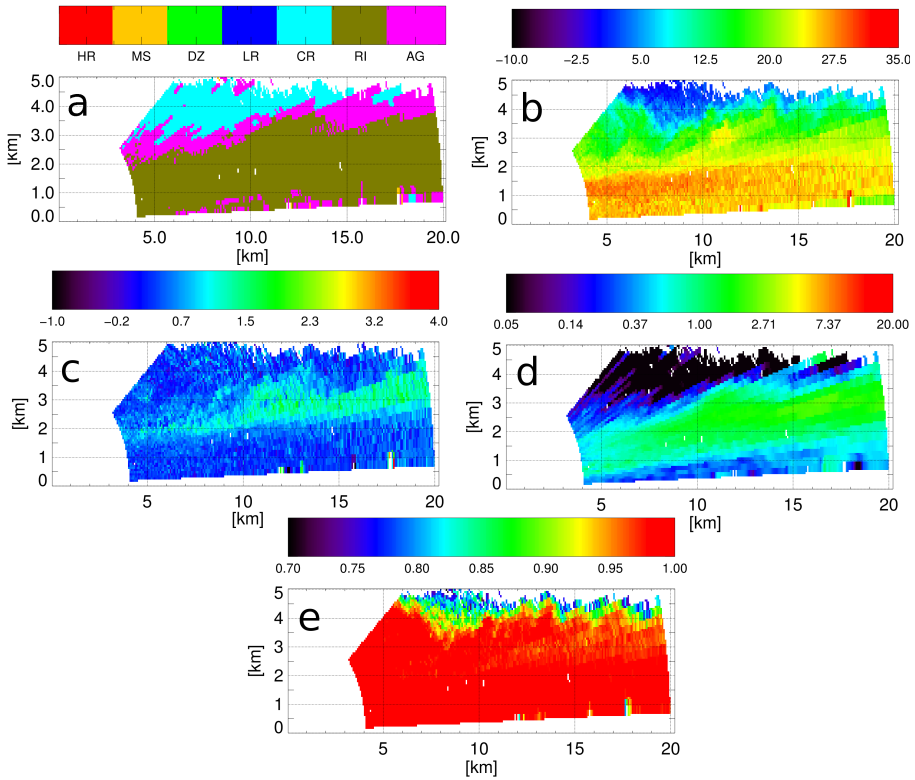

Figure 13. As in Fig. 8, for the snowfall event of the 26 March 2010, at 15:31 UTC in Davos (CH). The altitude of the radar is here 2133 m.

AMTD
7, 8465–8519, 2014

Hydrometeor classification from polarimetric radar measurements: a clustering approach

J. Grazioli et al.

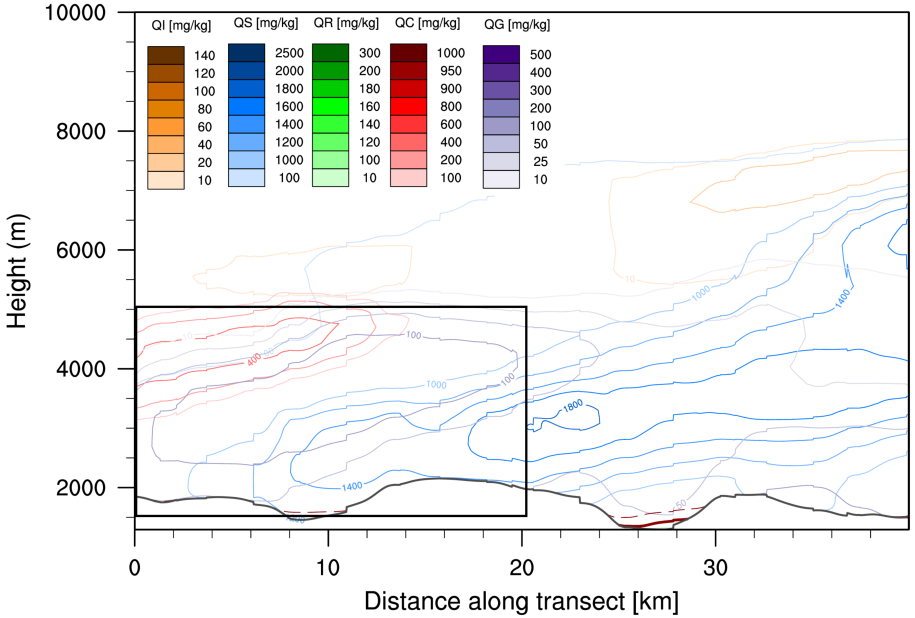

Figure 14. Mixing ratios of hydrometeor contents obtained with the COSMO2 numerical weather model along the RHI transect of MXPol (Same as Fig. 13), the 26 March 2010 at 15:29 UTC. Mixing ratios are given for cloud ice (QI), snow (QS), rain (QR), cloud water (QC), graupel (QG). The domain of Fig. 13 is highlighted by a black rectangle.

AMTD
7, 8465–8519, 2014

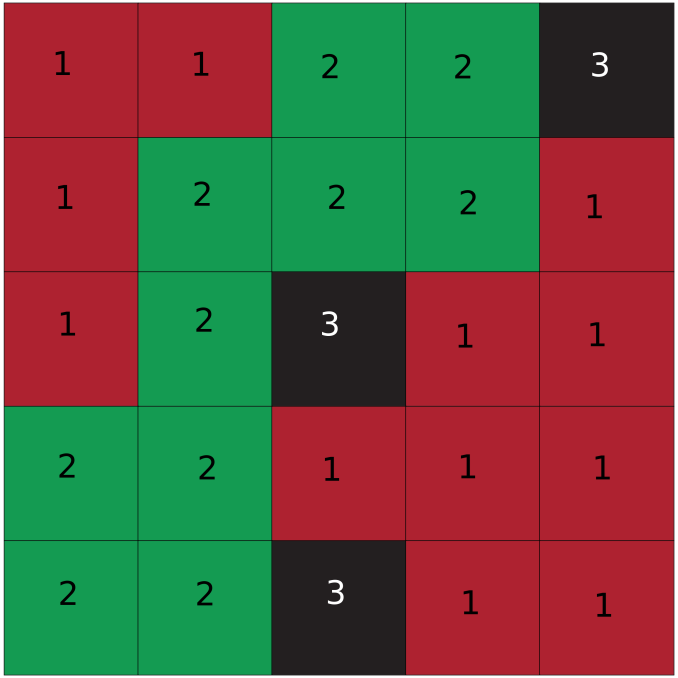

Figure A1. Schematic example to illustrate the spatial smoothness of a classification of a 5 × 5 pixels domain among three available classes. The classes are both color-coded and labeled as 1, 2 and 3.

AMTD
7, 8465–8519, 2014